

Atomic-Level Microstructure of Efficient Formamidinium-Based Perovskite Solar Cells Stabilized by 5-Ammonium Valeric Acid Iodide Revealed by Multinuclear and Two-Dimensional Solid-State NMR

Anwar Q. Alanazi,[†] Dominik J. Kubicki,^{*,†,‡,§,◆} Daniel Prochowicz,^{†,§} Essa A. Alharbi,[†] Marine E. F. Bouduban,[†] Farzaneh Jahanbakhshi,[∇] Marko Mladenović,^{∇,○} Jovana V. Milić,[†] Fabrizio Giordano,[†] Dan Ren,[†] Ahmed Y. Alyamani,^{||} Hamad Albrithen,^{||,#} Abdulrahman Albadri,^{||} Mohammad Hayal Alotaibi,^{||} Jacques-E. Moser,[⊥] Shaik M. Zakeeruddin,[†] Ursula Rothlisberger,[∇] Lyndon Emsley,^{*,†,§} and Michael Grätzel^{*,†}

[†]Laboratory of Photonics and Interfaces, Institute of Chemical Sciences and Engineering, School of Basic Sciences, Ecole Polytechnique Fédérale de Lausanne, CH-1015 Lausanne, Switzerland

[‡]Laboratory of Magnetic Resonance, Institute of Chemical Sciences and Engineering, School of Basic Sciences, Ecole Polytechnique Fédérale de Lausanne, CH-1015 Lausanne, Switzerland

[§]Institute of Physical Chemistry, Polish Academy of Sciences, Kasprzaka 44/52, 01-224 Warsaw, Poland

^{||}National Center for Nanotechnology, King Abdulaziz City for Science and Technology, P.O. Box 6086, Riyadh 11442, Saudi Arabia

[⊥]Photochemical Dynamics Group, Institute of Chemical Sciences and Engineering, Centre for Ultrafast Science, École Polytechnique Fédérale de Lausanne CH-1015 Lausanne, Switzerland

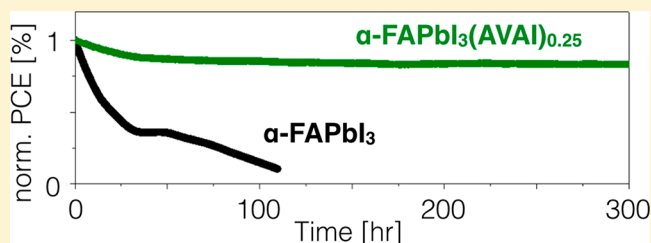
[#]Physics and Astronomy Department-Research Chair for Tribology, Surface and Interface Sciences, College of Science, and King Abdullah Institute for Nanotechnology-Aramco Laboratory for Applied Sensing Research, King Saud University, P.O. Box 2455, Riyadh 11451, Saudi Arabia

[∇]Laboratory of Computational Chemistry and Biochemistry (LCBC), École Polytechnique Fédérale de Lausanne (EPFL), CH-1015 Lausanne, Switzerland

[○]Scientific Computing Laboratory, Center for the Study of Complex Systems, Institute of Physics Belgrade, University of Belgrade, Pregrevaica 118, 11080 Belgrade, Serbia

Supporting Information

ABSTRACT: Chemical doping of inorganic–organic hybrid perovskites is an effective way of improving the performance and operational stability of perovskite solar cells (PSCs). Here we use 5-ammonium valeric acid iodide (AVAI) to chemically stabilize the structure of α -FAPbI₃. Using solid-state MAS NMR, we demonstrate the atomic-level interaction between the molecular modulator and the perovskite lattice and propose a structural model of the stabilized three-dimensional structure, further aided by density functional theory (DFT) calculations. We find that one-step deposition of the perovskite in the presence of AVAI produces highly crystalline films with large, micrometer-sized grains and enhanced charge-carrier lifetimes, as probed by transient absorption spectroscopy. As a result, we achieve greatly enhanced solar cell performance for the optimized AVA-based devices with a maximum power conversion efficiency (PCE) of 18.94%. The devices retain 90% of the initial efficiency after 300 h under continuous white light illumination and maximum-power point-tracking measurement.



INTRODUCTION

Hybrid organic–inorganic lead halide perovskites have received considerable attention since their first application to solar cells in 2009¹ and have recently reached a remarkable power conversion efficiency (PCE) above 24%.² These semiconducting materials have emerged as efficient light harvesters due to their easy fabrication process and unique

physicochemical properties such as low band gaps, high extinction coefficients, and high carrier mobilities.^{3–6} The most widely used 3D perovskites are methylammonium (MA) lead iodide MAPbI₃ and formamidinium (FA) lead iodide α -

Received: July 11, 2019

Published: October 8, 2019

FAPbI₃ with band gaps of around 1.5–1.6 and 1.48 eV, respectively.^{7,8} This alternation in band gap is very important in view of the Shockley-Queisser efficiency limit,⁹ which states that materials with a band gap around 1.4 eV are expected to have optimal light-harvesting ability in solar cell applications. In this respect, α -FAPbI₃ is a very promising material since it shows a near optimal band gap leading to maximal predicted power conversion efficiency. However, a major disadvantage of α -FAPbI₃ is its thermodynamic instability; the black perovskite phase of α -FAPbI₃ is thermodynamically stable only above 150 °C and spontaneously transforms to the wide-band-gap hexagonal, nonperovskite yellow δ -phase at room temperature.^{10–12} These shortcomings have been tackled by compositional engineering, for example, by mixing FA⁺ with smaller A-site cations such as MA^{+13–15} or Cs⁺,^{16–18} and through the introducing of mixed halide compositions.^{19,20} Another emerging approach to overcome the stability issue consists of applying lower-dimensional perovskites (2D and 2D/3D hybrids) formed by replacing the A-site cation with bulkier molecules such as longer alkylammonium chains.^{21,22} This approach is particularly interesting in terms of enhancing the stability of the structure against humidity, as these compounds generally exhibit higher resistance to the incorporation of water into the crystal structure.²³ Therefore, a number of large aliphatic alkylammonium cations, e.g., cyclopropylammonium (CA),²⁴ poly(ethylenimine) (PEI),²⁵ phenylethylammonium (PEA),^{26–28} or butylammonium (BA)^{29–31} have been intercalated into MAPbI₃ crystal lattice forming 2D/3D (also referred to as quasi-3D) hybrid perovskites with improved ambient stability. Alternatively, large-sized organic molecules with bifunctional groups can be utilized as additives to improve the crystallinity and stability of Pb-based perovskites by potentially cross-linking neighboring perovskite grains through strong hydrogen bonding.^{32–37} For example, the bifunctional alkylphosphonic acid ω -ammonium cation was hypothesized to be a cross-linking agent for facilitating the growth of perovskite crystals and forming high-performance and stable perovskite solar cells (PSCs).³² The use of bifunctional passivation ligands has also been demonstrated for perovskite nanocrystals.^{38,39} In a similar vein, oleate-capped all-inorganic perovskite nanocrystals have been demonstrated as a passivation agent for microcrystalline MAPbI₃ thin films.⁴⁰ Recently, the incorporation of a bifunctional salt of 5-ammonium valeric acid iodide (AVAI) has been reported to enhance crystallinity and stability of MAPbBr₃³³ and FASnI₃.³⁵ These cations are suggested to cross-link and as such play an important role in reducing the surface energy and passivating surface defects, which subsequently enhances the performance and operational stability of the devices.

Here, we report an effective one-step solution deposition method for the preparation of a high quality and stable α -FAPbI₃ perovskite active layer using the bifunctional organic molecule AVAI that acts as a structure-directing cross-linking agent between adjacent grains in the perovskite structure. Using solid-state NMR, we reveal that AVAI interacts with α -FAPbI₃ on the atomic level by binding to the 3D perovskite through hydrogen bonding interaction and stabilizing it against the detrimental α -to- δ phase transition. The introduction of AVAI to the perovskite precursor solution leads to the growth of highly crystalline films with large, micrometer-sized grains and enhanced charge-carrier lifetime. As a result, the optimized AVA-based mesoscopic heterojunction PSC yields a high PCE

of 18.94% and high operational stability after 300 h under continuous illumination.

EXPERIMENTAL SECTION

Materials. All materials were purchased from Sigma-Aldrich and used as received, unless stated otherwise. Perovskite powders for solid-state NMR studies were synthesized by grinding precursors in an electric ball mill (Retsch Ball Mill MM-200, agate grinding jar with a volume of 10 mL and 1 agate ball, diameter size 10 mm) for 30 min at 25 Hz. The precursors were packed in a glovebox under an argon atmosphere. After milling, the resulting powders were annealed at 140 °C for 10 min to reproduce the thin-film synthetic procedure. FAPbI₃: 0.172 g of FAI (1 mmol) and 0.461 g of PbI₂ (1 mmol); FAPbI₃(AVAI)_{0.25}: 0.172 g of FAI (1 mmol), 0.461 g of PbI₂ (1 mmol), and 0.029 g of AVAI (0.25 mmol).

Solar Cell Preparation. Fluorine-doped tin oxide (FTO) glass substrates (TCO glass, NSG 10, Nippon sheet glass, Japan) were etched from the edges by using Zn powder and 4 M HCl and then were cleaned by ultrasonication in Hellmanex (2%, deionized water), rinsed thoroughly with deionized water and ethanol, and then treated in oxygen plasma for 15 min. A 30 nm blocking layer (TiO₂) was deposited on the cleaned FTO by spray pyrolysis at 450 °C using a commercial titanium diisopropoxide bis(acetylacetonate) solution (75% in 2-propanol, Sigma-Aldrich) diluted in anhydrous ethanol (1:9 volume ratio) as precursor and oxygen as a carrier gas. A mesoporous TiO₂ layer was deposited by spin-coating a paste (Dyesol 30NRD) diluted with ethanol (1:6 wt ratio) (4000 rpm, acceleration 2000 rpm for 20 s) onto the substrate containing the TiO₂ compact layer and then sintered at 450 °C for 30 min in dry air.

Deposition of Perovskite Films. The perovskite films were deposited using a single-step deposition method from the precursor solution. The precursor solution of FAPbI₃ was prepared in argon atmosphere by dissolving equimolar amounts of PbI₂ and FAI in an anhydrous DMF/DMSO (4:1 (volume ratio)) mixture at a concentration of 1.4 M. Next, we added AVAI into the FAPbI₃ precursor solution using different molar ratios, resulting in several FAPbI₃(AVAI)_x compositions ($x = 0.05, 0.10, 0.25, 0.50$). The device fabrication was carried out under controlled atmospheric conditions with humidity < 2%. The precursor solution was spin-coated onto the mesoporous TiO₂ films in a two-step program at 1000 and 6000 rpm for 10 and 30 s, respectively. During the second step, 200 μ L of chlorobenzene was dropped on the spinning substrate 10 s prior the end of the program. This was followed by annealing the films at 150 °C for 30–40 min. After preparing the initial perovskite layer (control) as described above, the film was cooled down at room temperature. For completing the fabrication of devices, 90 mg of 2,2',7,7'-tetrakis(*N,N*-di-*p*-methoxyphenylamine)-9,9-spirobifluorene (spiro-OMeTAD) was dissolved in 1 mL of chlorobenzene as a hole-transporting material (HTM). The HTM was deposited by spin-coating at 4000 rpm for 20 s. The HTM was doped with bis(trifluoromethylsulfonyl)imide lithium salt (17.8 μ L prepared by dissolving 520 mg of LiTFSI in 1 mL of acetonitrile) and 28.8 μ L of 4-*tert*-butylpyridine. Finally, an \sim 80 nm gold (Au) layer was thermally evaporated.

Solid-State NMR Measurements. Room temperature ¹H (900.0 MHz) NMR spectra were recorded on a Bruker Avance Neo 21.1 T spectrometer equipped with a 3.2 mm CPMAS probe. ¹H and ¹³C chemical shifts were referenced to solid adamantane ($\delta_{\text{H}} = 1.91$ ppm and $\delta_{\text{C}} = 29.45$ (CH) and 38.48 (CH₂) ppm). ¹⁴N spectra were referenced to solid NH₄Cl (0 ppm) at 298 K. ²H spectra were referenced based on the ¹H chemical shift of NH₃⁺ in the nondeuterated AVA₂PbI₄. Recycle delays of 0.1 s (¹⁴N), 2.5–25 s (¹H–¹³C), and 0.25–2 s (²H) were used. Longitudinal relaxation times (T_1) were measured using a saturation-recovery sequence. ¹H–¹H spin diffusion measurements at 20 kHz MAS were carried out using a mixing period of 100 ms and a recycle delay of 5 s.

RESULTS AND DISCUSSION

The hybrid perovskite films were prepared by solution processing. The precursor solution of FAPbI₃ was prepared by dissolving equimolar amounts of PbI₂ and FAI in a DMF/DMSO (4:1 v/v) mixture at a concentration of 1.4 M. Next, we added AVAI into the FAPbI₃ precursor solution using different molar ratios, resulting in several FAPbI₃(AVAI)_x compositions ($x = 0.05, 0.10, 0.25, 0.50$). We first evaluated the photovoltaic performance of films fabricated by a one-step antisolvent deposition method (for more details of perovskite film formation, see the [Experimental Section](#)). The solar cells were fabricated using the following architecture: glass/FTO/compact-TiO₂/mesoporous TiO₂/perovskite/Spiro-OMeTAD/Au.

The characteristic $J-V$ curves for the champion FAPbI₃(AVAI)_x-based devices measured under reverse voltage scan are shown in [Figure 1a](#). The reference PSCs ($x = 0$) yielded

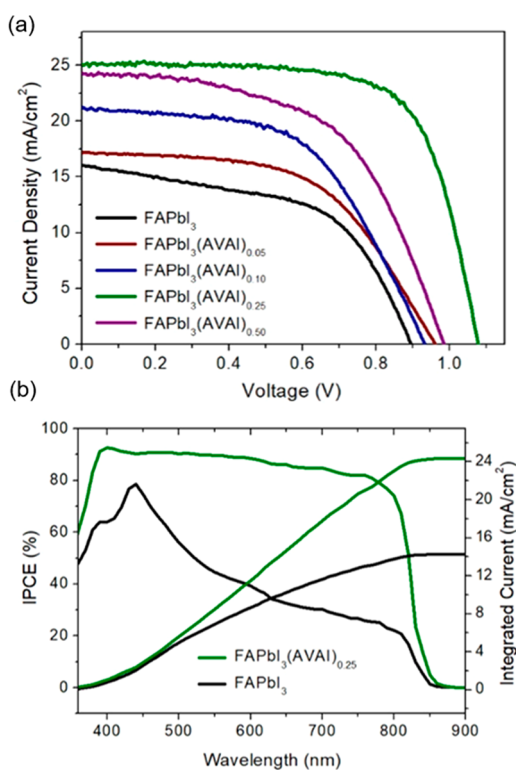


Figure 1. Photovoltaic characterization of the devices. (a) Comparison of the $J-V$ curves for the champion FAPbI₃(AVAI)_x ($x = 0, 0.05, 0.10, 0.25, 0.50$) devices. (b) IPCE and integrated J_{sc} of the α -FAPbI₃ and FAPbI₃(AVAI)_{0.25} devices.

poor device performance, with a maximum PCE of 7.26%, V_{oc} of 0.88 V, J_{sc} of 15 mA cm⁻², and fill factor (FF) of 55%. We found that the device performance increases monotonically with the amount of added AVAI up to 25% (abbreviated as FAPbI₃(AVAI)_{0.25}), achieving a maximum PCE of 18.94% with a V_{oc} of 1.07 V, J_{sc} of 25.1 mA cm⁻², and FF of 70%. The integrated J_{sc} calculated from the IPCE spectrum of the FAPbI₃(AVAI)_{0.25} device equals to 24.20 mA cm⁻², which is within 3% of the J_{sc} measured under AM 1.5G standard irradiation ([Figure 1b](#)). A further increase in the AVAI content up to 50% deteriorates all figures of merit with PCE declining to 13.22%. [Table 1](#) shows a summary of the photovoltaic parameters for the champion devices with different AVAI

Table 1. Comparison of Photovoltaic Parameters for Champion FAPbI₃(AVAI)_x Devices ($x = 0, 0.05, 0.10, 0.25, 0.50$) with Backward Scan Direction

perovskite	V_{oc} [V]	J_{sc} [mA/cm ²]	FF	PCE [%]
FAPbI ₃	0.88	15.0	0.55	7.26
FAPbI ₃ (AVAI) _{0.05}	0.89	17.2	0.55	9.15
FAPbI ₃ (AVAI) _{0.10}	0.89	23.9	0.52	11.67
FAPbI ₃ (AVAI) _{0.25}	1.08	25.1	0.70	18.94
FAPbI ₃ (AVAI) _{0.50}	0.98	24.3	0.55	13.22

doping levels. The maximum power point (MPP) of the FAPbI₃(AVAI)_{0.25} device shows the stabilized PCE of 17.70% after 300 s of continuous illumination ([Figure S1](#)). The photovoltaic performance figures of merit are listed in [Figure S2](#) for the control FAPbI₃ and FAPbI₃(AVAI)_x ($x = 0.05, 0.10, 0.25, 0.50$) devices. The increase in PCE upon AVAI doping is mainly due to the large improvement of all photovoltaic metrics, i.e., J_{sc} , V_{oc} , J_{sc} , and FF, which can be attributed to improved phase purity, perovskite film morphology, and longer charge carrier lifetimes, as well as reduced defect density (vide infra). Notably, the efficiency of the champion FAPbI₃(AVAI)_{0.25} device is among the highest reported for α -FAPbI₃-based solar cells.^{41,42} $J-V$ hysteresis and its suppression have been important subjects of research in the field of PSCs.⁴³ We have found that both the reference and FAPbI₃(AVAI)_{0.25} PSCs display hysteresis ([Figure S9](#) and [Table S2](#)). We therefore conclude that AVAI does not lead to its suppression.

To investigate the crystallinity of the AVAI-doped perovskite, we measured powder X-ray diffraction (pXRD) of films deposited onto mesoporous-TiO₂/compact layer TiO₂/FTO ([Figure 2a](#)). The reference α -FAPbI₃ and the FAPbI₃(AVAI)_x films have a very similar structure, with the peaks at $\sim 14.0^\circ$ and $\sim 28.0^\circ$ originating from the (110) and (220) planes of the 3D perovskite phase. The reference α -FAPbI₃ film also exhibits a strong peak at 11.6° along with a number of low-intensity peaks in the 25–40° region, corresponding to the hexagonal nonperovskite δ -FAPbI₃ phase.¹⁰ The δ -phase peaks disappear upon AVAI addition and are absent in all the FAPbI₃(AVAI)_x films. We note that AVA-rich iodoplumbate phases (yielding peaks below $2\theta = 10^\circ$) are also absent.³⁴ Furthermore, the overall diffraction intensity is enhanced with increased amounts of AVAI doping, indicative of improved crystallinity. The relative intensity of the two perovskite peaks changes very slightly as the AVAI content increases. This might be related to preferred orientation effects which have been previously observed in other amino acid doped perovskite thin films and ascribed to amino acid-TiO₂ anchoring.⁴⁴ We note that there are no diffraction peaks corresponding to the AVA dopant. This is consistent with the pronounced dynamic disorder of AVA evidenced by ²H MAS NMR (vide infra). This is correlates with the SEM measurements which show that the average grain size in the FAPbI₃(AVAI)_x films systematically increases from a few hundred nanometers to about a micrometer with increasing AVAI doping level ([Figure S3](#)). This result suggests that AVAI interacts with α -FAPbI₃ to facilitate crystal growth during annealing. We note that the largest crystallite size was obtained for the 50% AVAI composition which, however, showed a decrease in the J_{sc} , V_{oc} , and FF. This translated to lower PCE, likely due to an increase in the internal resistance of the devices with an excessive AVAI content, analogous to the result previously

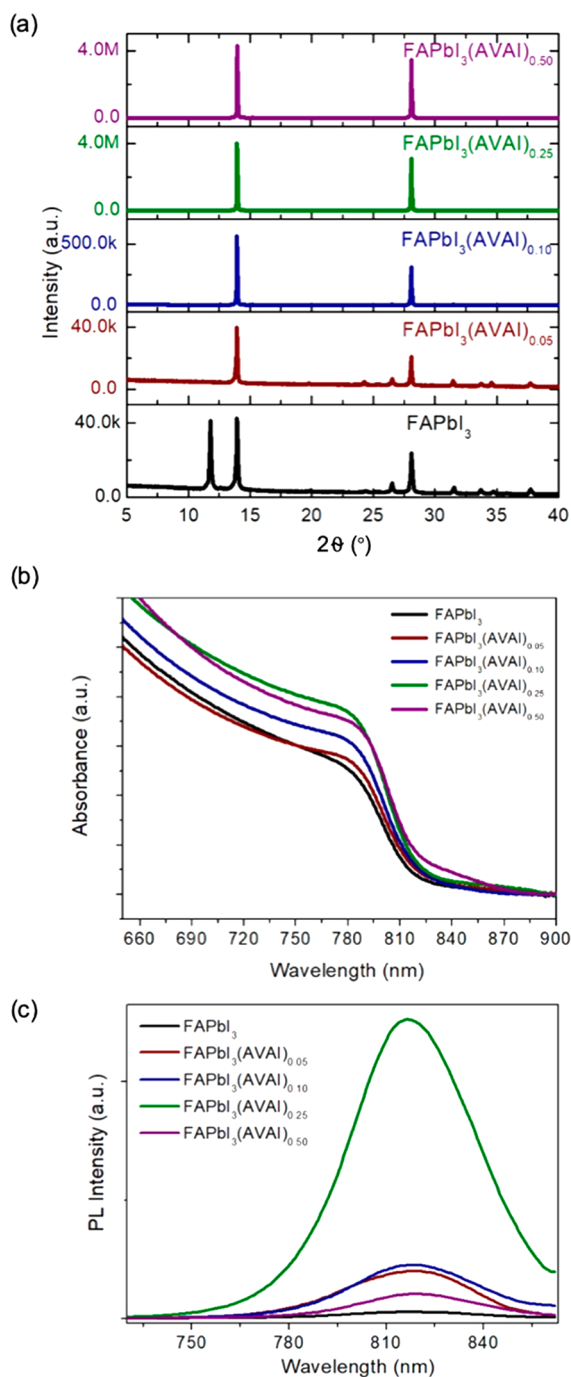


Figure 2. Characterization of the $\text{FAPbI}_3(\text{AVAI})_x$ perovskite films. (a) Powder XRD patterns, (b) UV–vis absorption, and (c) steady-state PL spectra.

observed for PEA.²⁸ Further, we tested hydrophobicity of the FAPbI_3 and $\text{FAPbI}_3(\text{AVAI})_{0.25}$ films by measuring the contact angle of a water droplet (Figure S10). The contact angle increases from 46.2° to 59.2° after AVA doping, indicating higher hydrophobicity of the AVA-doped material.

The effects of the changes in the structural features and morphology on the optoelectronic properties were assessed by means of UV–vis absorption and photoluminescence (PL) absorption spectroscopy. The UV–vis absorption spectra of the $\text{FAPbI}_3(\text{AVAI})_x$ films deposited on glass are shown in Figure 2b. We find that the band edges of the absorption spectra very slightly red-shift (~ 2 nm) when the content of

AVAI is increased. In addition, steady-state PL spectra show a correspondingly small red shift for the $\text{FAPbI}_3(\text{AVAI})_{0.50}$ film with respect to the reference FAPbI_3 (Figure 2c), consistent with the UV–vis measurements. The red shift in both UV–vis and PL spectra might be caused by the increased crystallinity and larger grain size,⁴⁵ consistent with the SEM images, and/or due to the formation of a new chemical compound. These observations are qualitatively different from the previous result, where the absorbance and PL peaks of AVA-doped perovskite films blue-shifted with increasing AVABr amount due to the introduction of Br into the perovskite structure.³³

To further confirm the beneficial effect of the addition of AVAI to the FAPbI_3 composition, transient absorption (TA) spectroscopy measurements were performed on both a reference FAPbI_3 and $\text{FAPbI}_3(\text{AVAI})_{0.25}$ films deposited on glass slides. Figure 3a shows TA dynamics of the ground-state

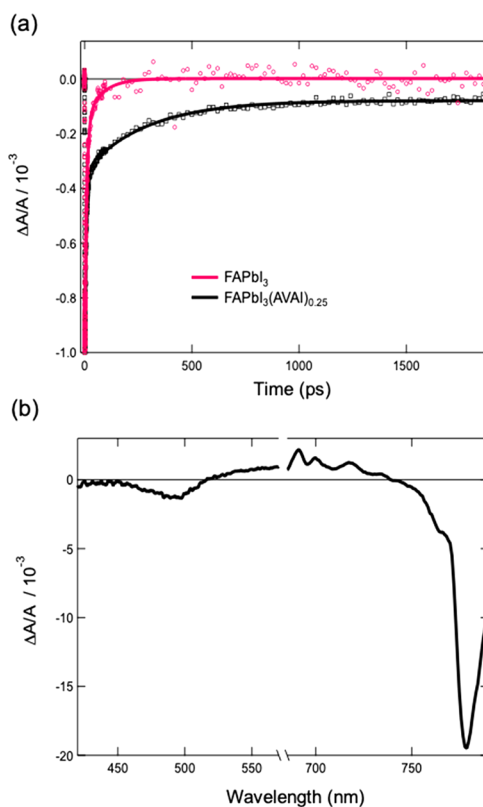


Figure 3. (a) Ground-state bleaching (760 nm) and stimulated emission dynamics obtained by transient absorption with $l_{\text{ex}} = 390$ nm, at an excitation fluence $F = 250$ nJ. (b) Transient absorbance spectra of $\text{FAPbI}_3(\text{AVAI})_{0.25}$ measured under the same conditions as in (a).

bleaching (GSB) and stimulated emission (SE) signals, which closely overlap in the band-edge region (760 nm) for both films (Figure 3b). The GSB signal is related to the filling of the bands due to photoexcitation with its decay corresponding to the depletion of the conduction band and/or the filling of the valence band by electrons. As such, it reflects both charge recombination and charge extraction to a selective contact layer. We note that GB bleaching recovery reflects contributions from both radiative and nonradiative carrier recombination. On the other hand, the dynamics of the SE signal describes only radiative electron–hole recombination. Since the samples were prepared with no extracting layers, it follows

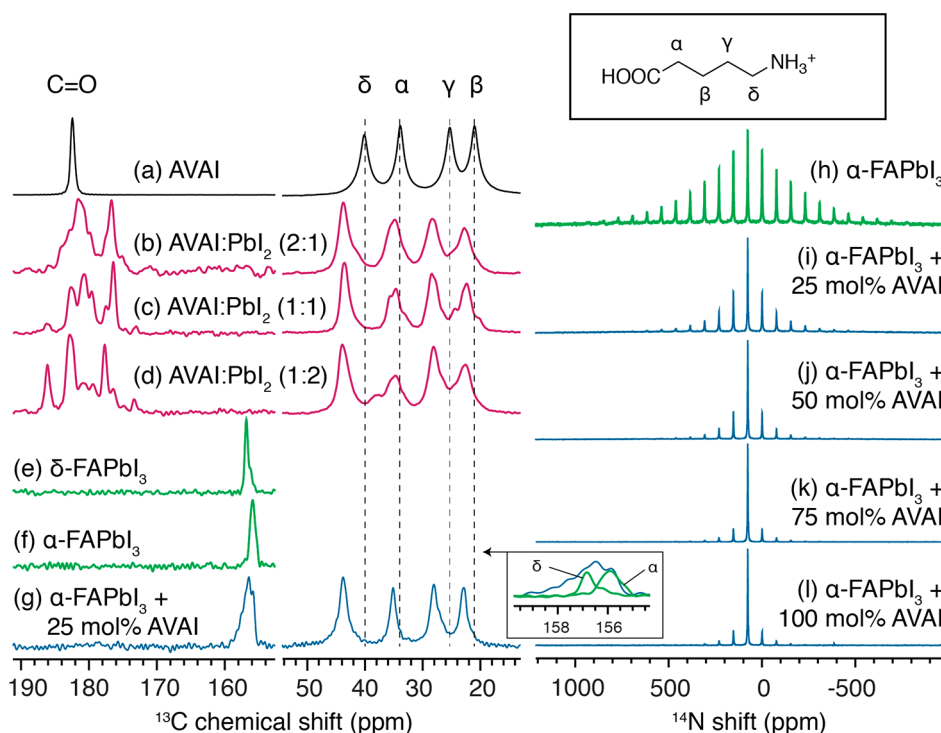


Figure 4. Solid-state MAS NMR characterization of the bulk mechanochemical materials. ^1H - ^{13}C CP spectra at 21.1 T, 298 K, and 20 kHz MAS of (a) neat AVAI (the structure is shown in the inset), (b) AVAI:PbI₂ (2:1 mol/mol), (c) AVAI:PbI₂ (1:1 mol/mol), (d) AVAI:PbI₂ (1:2 mol/mol), (e) δ -FAPbI₃, (f) α -FAPbI₃, and (g) α -FAPbI₃ + 25 mol % AVAI. The inset shows a horizontal zoom of the FA region in panels (e)–(g). ^{14}N MAS NMR spectra at 21.1 T, 298 K, and 5 kHz MAS of (h) α -FAPbI₃, and α -FAPbI₃ doped with (i) 25 mol % AVAI, (j) 50 mol % AVAI, (k) 75 mol % AVAI, and (l) 100 mol % AVAI.

that comparing the decay rates of the GSB+SE signals for FAPbI₃ versus FAPbI₃(AVAI)_{0.25} is directly related to charge carrier lifetimes in these materials. Clearly, the addition of AVAI results in a significantly slower decay rate and the second decay component is almost four times larger for FAPbI₃(AVAI)_{0.25} than in FAPbI₃ (286 ps vs 76 ps) (Table S1). We note that the long time contribution in the case of FAPbI₃(AVAI)_{0.25} most likely arises from Shockley–Read–Hall pseudo-first-order recombination via charge carrier trapping states.

We employed X-ray photoelectron spectroscopy (XPS) to verify if the surface of the FAPbI₃ film is modified during treatment with AVAI. The comparison of the Pb 4f, C 1s, N 1s, and O 1s XPS peaks for the AVAI, AVAI:PbI₂ (2:1), α -FAPbI₃, and FAPbI₃(AVAI)_{0.25} films is shown in Figure S4.

The O 1s spectrum of the AVAI film shows a peak at 532.2 eV, which can be assigned to the binding energy of C–O and C=O in the carboxylate group of AVAI. The O 1s spectrum of the 2:1 AVAI:PbI₂ film shifts toward lower binding energy by 0.41 eV (maximum at 531.82 eV), while the corresponding peak of FAPbI₃(AVAI)_{0.25} shifts to a higher energy by 0.7 eV (maximum at 532.9 eV) compared to the pure AVAI film. This indicates that AVAI is involved in a new chemical interaction with α -FAPbI₃ rather than exists as a separate AVAI-based iodoplumbate phase on the surface of the perovskite film. A full discussion of the XPS data is given in the Supporting Information.

In order to elucidate the atomic-level microstructure of the AVAI-doped α -FAPbI₃ compositions, we carried out multinuclear solid-state NMR measurements on materials prepared by mechanochemistry.^{15,46,47} We and others have recently shown the broad applicability of solid-state NMR to lead

halide perovskites^{48–61} and its utility in assessing the interaction of small organic molecules with the hybrid perovskite phases.^{62–64}

Figure 4a shows a ^{13}C spectrum of neat AVAI which contains five resonances corresponding to the following molecular fragments: C=O (182.4 ppm), δ -CH₂ (40.1 ppm), α -CH₂ (33.8 ppm), γ -CH₂ (25.3 ppm), and β -CH₂ (21.0 ppm). The material formed in a reaction between AVAI and PbI₂ has been hypothesized to be a 2D (AVA)₂PbI₄ perovskite;⁶⁵ however, to the best of our knowledge, its crystal structure has not been solved to date. A perfectly ordered Ruddlesden–Popper (RP) (AVA)₂PbI₄ structure would be expected to possess exactly one type of carbonyl atom inside the unit cell. Here, we find that, in the reaction between AVAI and PbI₂, depending on the molar ratio of the two components, up to eight distinct C=O environments are formed (Figure 4b–d for AVAI:PbI₂ ratios of 2:1, 1:1, and 1:2, respectively). In addition, the aliphatic signals of AVAI are shifted with respect to neat AVAI in all three compositions, confirming that AVAI has fully reacted in all three cases. This type of structural complexity is expected in structures capable of forming recombinant analogues (polytypes) with different stacking sequences, with (β -alaninium)₂SnI₄ being a structurally closely related example.⁶⁶ We therefore highlight that the AVAI–PbI₂ phase system cannot be considered as a simple RP phase, and further single crystal studies are necessary to develop its full understanding.

^{13}C MAS NMR also makes it possible to distinguish between δ -FAPbI₃ (156.8 ppm, Figure 4e) and α -FAPbI₃ (155.9 ppm, Figure 4f).⁵⁰ The material formally corresponding to α -FAPbI₃ mixed with 25 mol % AVAI (Figure 4g) reveals a new broad signal (156.5 ppm) corresponding to a carbon environment in

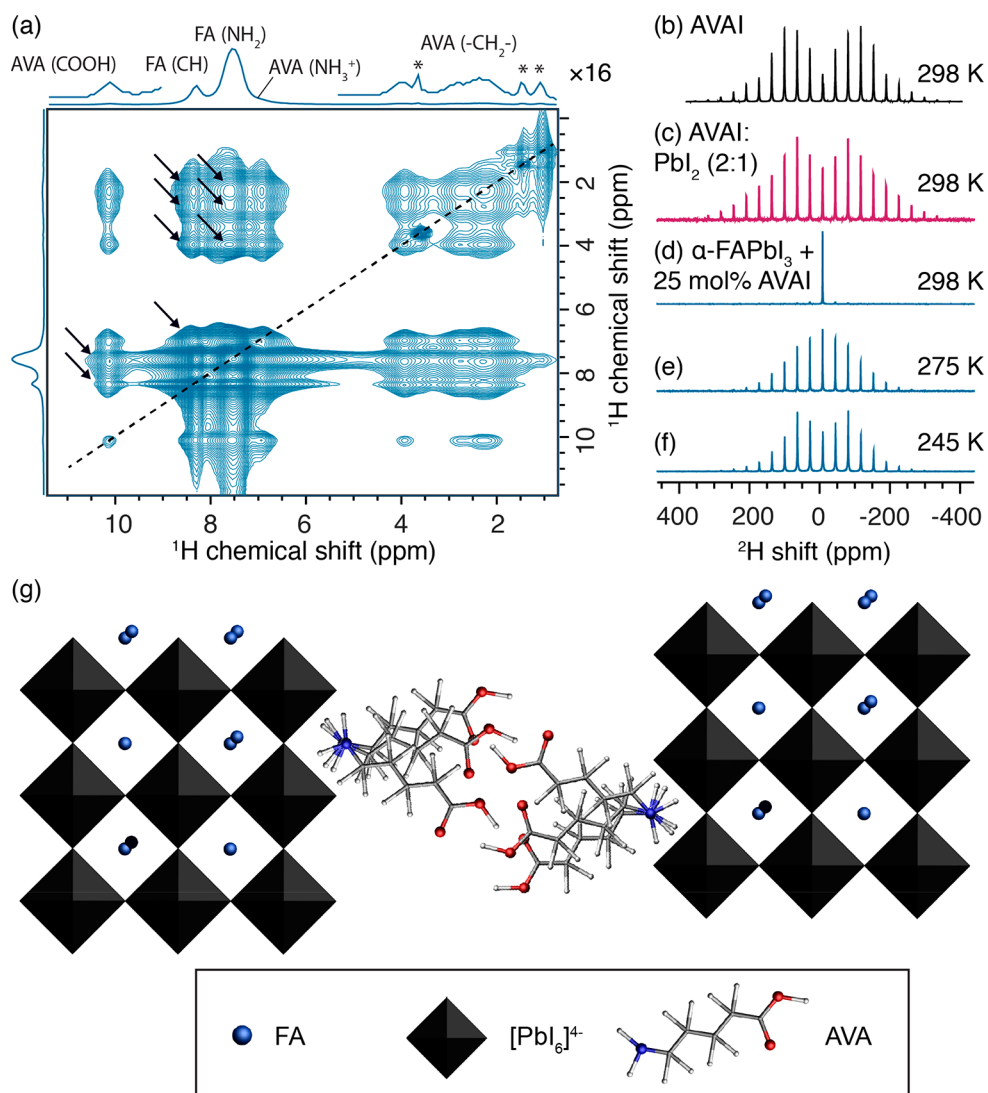


Figure 5. Solid-state MAS NMR characterization of the bulk mechanochemical materials. (a) ^1H – ^1H spin-diffusion measurement at 21.1 T, 298 K, and 20 kHz MAS (mixing time of 100 ms). The aliphatic region has been magnified 16-fold. The asterisks mark trace aliphatic impurities. ^2H MAS NMR at 21.1 T and 5 kHz MAS of (b) neat AVAI, (c) AVAI: PbI_2 (2:1 mol/mol), and α -FAPbI₃ + 25 mol % AVAI at (d) 298 K, (e) 275 K, and (f) 245 K. (g) Structural model of the AVAI-modified α -FAPbI₃ proposed based on the solid-state NMR data.

which FA interacts with AVA on the atomic level. The aliphatic signals of AVA are, again, shifted with respect to neat AVAI, confirming that the precursor has fully reacted to form a new chemical compound. The C=O signals are not visible in this case due to dynamics, as discussed below. We subsequently investigated whether or not the presence of AVAI leads to any changes in the 3D perovskite structure of α -FAPbI₃. ^{14}N MAS NMR is a sensitive probe of cubooctahedral symmetry in 3D perovskites, which determines the breadth of the ^{14}N spinning sideband (SSB) manifold, with narrower manifolds corresponding to a more symmetric (closer to cubic) environment of the A-site cation reorienting on the picosecond time scale.^{50,63} The ^{14}N MAS NMR spectrum of α -FAPbI₃ is characterized by a central peak at 75.9 ppm, surrounded by 11 orders of spinning sidebands (Figure 4h). α -FAPbI₃ doped with 25 mol % AVAI shows no change to the central peak position but the number of visible SSB orders decreases to 7. As the AVAI doping level is increased to 50, 75, and 100 mol % (excess with respect to FAPbI₃), the number of visible SSB orders decreases to 5, 4, and 3, respectively (Figure 4i–l,

respectively). This narrowing of the ^{14}N SSB envelope upon AVAI doping suggests that AVAI changes the intrinsic cubooctahedral symmetry of the α -FAPbI₃ phase so as to make it closer to cubic. We have previously observed similar structure directing effects in the case of 3-(5-mercapto-1H-tetrazol-1-yl)benzenaminium iodide⁶² and adamantylammonium iodide.⁶³ On the other hand, the opposite effect (SSB manifold broadening) is observed upon A-site cation mixing in lead halide perovskites based on MA/FA,⁵⁰ Cs/FA,⁵¹ MA/guanidinium,⁵⁷ and MA/dimethylammonium⁵⁶ mixtures.

In order to corroborate the atomic-level interaction between AVA and FA in AVAI-doped α -FAPbI₃, we carried out a two-dimensional ^1H – ^1H spin diffusion (SD) measurement, which correlates NMR signals based on the atomic-level proximity of the corresponding species for distances on the order of tens of Å through dipole–dipole couplings.⁶⁷ Figure 5a shows a ^1H – ^1H SD spectrum of α -FAPbI₃ doped with 25 mol % AVAI. The horizontal and vertical projections show a regular 1D ^1H spectrum with the structural assignments. Each peak in the 1D spectrum has a corresponding diagonal peak lying on the

dashed line. Off-diagonal cross peaks evidence close spatial proximity of the species giving rise to a specific set of diagonal peaks. The spectrum is symmetric around the diagonal. For example, there are cross peaks between the $-\text{CH}_2-$, $-\text{NH}_3^+$, and $-\text{COOH}$ signals of AVA, corresponding to intramolecular contacts. More interestingly, analogous contacts are visible between the CH and NH_2 groups of FA and all the signals belonging to AVA (indicated by arrows), unambiguously evidencing that *FA and AVA form a mixed phase and are interacting at the atomic level*. We note that AVA is too large to be incorporated as an A-site cation. That said, it could conceivably lead to a hollow perovskite structure characterized by large $[\text{PbI}_6]^{4-}$ octahedral vacancies.^{68,69} However, hollow perovskites exhibit significantly wider band gaps for a comparable amount of dopant while in our case the band gap remains nearly identical up to 50 mol % AVAI doping, excluding the possibility of hollow perovskite formation.

Having investigated the microstructure of the mixed FA/AVA phase, we now turn to the dynamics of AVA in this material. To that end, we use ^2H MAS NMR which is an excellent probe of dynamics in solids,⁷⁰ since the shape of the ^2H SSB manifold is determined by the available motional degrees of freedom of the reorienting molecular fragment. For example, the ^2H MAS NMR spectra of AVAI (Figure 5b) and AVAI:PbI₂ (2:1) (Figure 5c) have an SSB manifold characteristic of 3-fold (C_3) jumps of the $-\text{ND}_3^+$ group around the C–N bond, with the backbone of the molecule being rigid. The apparent quadrupolar coupling constant, C_Q , which can be extracted by fitting the spectra, has a value of 53 and 37 kHz for AVAI and AVAI:PbI₂ (2:1), respectively, and is typical for $-\text{ND}_3^+$ attached to an otherwise rigid molecular fragment.⁷¹ Structural rigidity in the case of AVA is expected and consistent with the strong intermolecular hydrogen bonding of the COOH groups, analogous to that observed in (β -alaninium)₂SnI₄,⁶⁶ and further corroborated by molecular dynamics simulations of the $n = 1$ Ruddlesden–Popper phase (vide infra). In contrast, the ^2H spectrum of α -FAPbI₃ doped with 25 mol % AVAI (Figure 5d) consists of a single line (apparent $C_Q \approx 0$ kHz), which means that in this case the $-\text{ND}_3^+$ group is reorienting isotropically (in a tetrahedral or lower symmetry) at a rate greater than 10^5 jumps per second.⁷⁰ This scenario is only possible if the whole AVA backbone has additional degrees of freedom, making it dynamically disordered. We note that this implies that the hydrogen bonding network is also labile and the H-bonds are cleaved and formed at a rate greater than 10^5 /s. Rigidity can be gradually reintroduced by cooling the material down to 275 K (Figure 5e) and 245 K (Figure 5f) (apparent C_Q of 34 and 49 kHz, respectively), at which point the only residual degree of freedom is again the 3-fold $-\text{ND}_3^+$ jump. Since dynamics partly averages out the ^1H – ^{13}C dipole–dipole couplings, the cross-polarization efficiency in AVA is expected to be lower.⁵⁰ This is indeed the case, as the C=O signal cannot be detected at room temperature (Figure 4g) but is readily detected at lower temperatures when rigidity is reintroduced (Figure 5s). To the best of our knowledge, this is the first demonstration of unrestricted reorientation of a molecular modifier used to stabilize a 3D perovskite. We believe that structural dynamics and lability will become an important design criterium for stable perovskites, once we have gained better understanding of its effects on the resulting photophysics. Based on the above results, we propose that the interaction between the perovskite and AVA is surface-based, as shown in Figure 5g. AVA binds to

the surface of α -FAPbI₃ through the terminal amino group, while the remaining carboxylate groups are dynamically disordered at room temperature, leading to dynamic formation and breaking of COOH...COOH hydrogen bonds between adjacent AVA molecules. This type of interaction can also conceivably lead to grain cross-linking.

While XRD does not provide insight into the long-range ordering of AVA in the doped FAPbI₃ structure, AVA has been previously reported to form Ruddlesden–Popper (RP) 2D structures with MA, $\text{AVA}_2(\text{MA})_{n-1}\text{PbI}_{3n+1}$.⁷² We therefore investigated the structural and electronic properties of the analogous RP series, $\text{AVA}_2(\text{FA})_{n-1}\text{PbI}_{3n+1}$, for $n = 1, 2, 3$ and ∞ as a potential structural candidate. For $n = 2$ and $n = 3$, the AVA and FA cations are in atomic-level contact (5–10 Å, similar to the materials studied experimentally by 2D NMR SD measurements) and we use these structures as model, computationally tractable systems, to complement the experimental findings. The initial structures were formed based on the RP structures of $\text{BA}_2(\text{MA})_{n-1}\text{PbI}_{3n+1}$.³⁰ The spacer configuration was taken from the structure of $\text{ABA}_2(\text{MA})_{n-1}\text{PbI}_{3n+1}$ (ABA = 4-aminobutyric acid)⁷² with a hydrogen bonding pattern between carboxylic groups of every two adjacent AVA molecules of opposite layers along the x direction (Figure S6b). Similar to the trend reported for band gaps in $\text{BA}_2(\text{MA})_{n-1}\text{PbI}_{3n+1}$ RP structure,³⁰ increasing the inorganic layer thickness (higher n values) reduces the band gap, which tends to the value of undoped α -FAPbI₃ as n increases. Accordingly, the band gap of AVAI-doped α -FAPbI₃ is essentially identical to that of neat α -FAPbI₃ (Figure 2b, c), since it can be considered as a high n representative of the RP $\text{AVA}_2(\text{FA})_{n-1}\text{PbI}_{3n+1}$ family. To provide additional insight into the experimental observation that AVA-doped α -FAPbI₃ is more cubic than α -FAPbI₃ (octahedral tilting angle closer to 90°), we calculated the distribution of octahedral tilting angles of the computationally optimized structure of α -FAPbI₃ taking also finite temperature effects into account. We performed 2 ps simulations at 300 K and obtained a time-averaged mean value of 89.9° with a standard deviation of 9.1°. Considering the relatively large standard deviation, the subtle templating effect of AVAI observed through ^{14}N MAS NMR (Figure 4h–l) is likely beyond the accuracy of the DFT MD runs. We in turn addressed the propensity of AVA to form strong intermolecular hydrogen bonds in the iodoplumbate AVA_2PbI_4 phase at room temperature, experimentally evidenced by ^2H MAS NMR (Figure 5c). To that end, we assessed the finite temperature impact on the DFT optimized 0 K structure. We performed a 6 ps Born–Oppenheimer molecular dynamics simulation of the material to investigate the motion of the spacer molecules, as well as the rigidity of the inorganic layers to which the spacers are anchored. We find that, on this time scale, the hydrogen bonding pattern is mostly preserved at 300 K (Figure 6a), consistent with the NMR result. To further understand how the AVA spacers are confined between the inorganic layers, we calculated the vertical penetration depth of AVA into the inorganic sublattice (Figure 6b), as measured by the average Pb–N distance along the normal of the closest PbI₂ plane, since this parameter has been reported to correlate with the octahedral distortion and phase transition temperatures.⁷³ We find that the penetration depth is mostly below 3.17 Å, which corresponds to the average vertical Pb–I distance, confirming that the spacers penetrate the inorganic sublattice. The rigidity of the spacers was studied by calculating the distribution of polar, θ , and azimuthal, φ , angles of the spacers, excluding

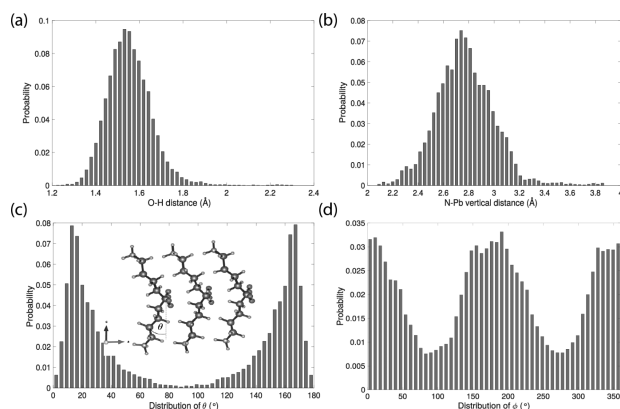


Figure 6. Thermal distributions at $T = 300$ K from 6 ps first-principles MD simulations. (a) Histogram of intermolecular O...H-bond distances between COOH groups of adjacent spacers of opposite layers, (b) Distribution of vertical penetration distances of NH_3^+ into the inorganic slab (measured as Pb–N distance along the normal of the closest PbI_2 plane). Distribution of (c) polar, θ , and (d) azimuthal, φ , angles of AVA in the spacer layers. The polar angle (denoted in the inset) is defined as the inclination of AVA with respect to the vertical c axis, and the azimuthal angle indicates the inclination of AVA (projection onto the ab plane) with respect to the a axis.

translation. The polar angle refers to the inclination of AVA with respect to the vertical axis, while the azimuthal angle is the planar deviation of AVA from the x axis. The polar angle distribution confirms that the spacers manifest a preferred orientation with respect to the vertical axis (Figure 6c) while showing a certain degree of rotation, yet maintaining their initial H-bond pattern (Figure 6d).

The effects of these structural properties on the long-term stability of the material were investigated by comparing the reference and $\text{FAPbI}_3(\text{AVAI})_{0.25}$ -based PSC under continuous 1.5 G irradiation ($100 \text{ mW}\cdot\text{cm}^{-2}$) and maximum power point tracking in a nitrogen atmosphere at room temperature. Figure S7 shows that the ambient stability of the $\text{FAPbI}_3(\text{AVAI})_{0.25}$ -based device is greatly improved as it retains 90% of its initial PCE up to 300 h. On the contrary, the PCE of the undoped α - FAPbI_3 device decays rapidly and reaches 10% of its initial efficiency within 100 h.

CONCLUSIONS

In conclusion, we have demonstrated that the bifunctional organic molecule AVAI can act as a molecular modulator that improves the stability of α - FAPbI_3 . We have elucidated and illustrated the atomic-level interaction between AVAI and the perovskite by applying multinuclear and two-dimensional solid-state NMR spectroscopy. We have found that AVAI displays a structure-directing role by forming hydrogen bonds with the perovskite lattice through its NH_3^+ group, while its COOH end is involved in dynamic hydrogen bonding with other AVA moieties, as further corroborated by DFT-based molecular dynamics simulations of fully periodic RP phases. These molecular features yield improved morphological and optoelectronic quality of the films. In particular, transient absorption measurements reveal significantly enhanced charge carrier lifetimes in the AVA-doped perovskite. As a result, the mesoscopic heterojunction photovoltaic solar cell demonstrated a high PCE of 18.94% and high operational stability after 300 h under continuous illumination. Our work illustrates that

molecular modulation of 3D perovskites using bifunctional modifiers is an effective way to simultaneously achieve high performing and stable FAPbI_3 -based PSCs.

ASSOCIATED CONTENT

Supporting Information

The Supporting Information is available free of charge on the ACS Publications website at DOI: 10.1021/jacs.9b07381.

Further experimental details, MPP tracking, J – V statistics, SEM images, XPS spectra, additional NMR spectra, and stability measurements (PDF)

AUTHOR INFORMATION

Corresponding Authors

*djk47@cam.ac.uk
 *lyndon.emsley@epfl.ch
 *michael.gratzel@epfl.ch

ORCID

Dominik J. Kubicki: 0000-0002-9231-6779
 Daniel Prochowicz: 0000-0002-5003-5637
 Farzaneh Jahanbakhshi: 0000-0001-7113-2746
 Jovana V. Milić: 0000-0002-9965-3460
 Dan Ren: 0000-0003-3738-6421
 Abdulrahman Albadri: 0000-0003-1579-0474
 Mohammad Hayal Alotaibi: 0000-0001-5435-5200
 Jacques-E. Moser: 0000-0003-0747-4666
 Ursula Rothlisberger: 0000-0002-1704-8591
 Lyndon Emsley: 0000-0003-1360-2572
 Michael Grätzel: 0000-0002-0068-0195

Present Address

♦D.J.K.: University of Cambridge, Cavendish Laboratory, J J Thomson Avenue, Cambridge CB3 0HE, United Kingdom.

Notes

The authors declare no competing financial interest.

ACKNOWLEDGMENTS

A.Q.A and E.A. gratefully acknowledge King Abdulaziz City for Science and Technology (KACST) for the fellowship. M.G. and S.M.Z. thank the King Abdulaziz City for Science and Technology (KACST) for the financial support. D.J.K. and L.E. acknowledge Swiss National Science Foundation Grants No. 200021_160112 and 200020_178860. D.P. acknowledges the financial support from the HOMING program of the Foundation for Polish Science cofinanced by the European Union under the European Regional Development Fund (POIR.04.04.00-00-SEE7/18-00). U.R. acknowledges funding from the Swiss National Science Foundation via the NCCR MUST, the Sinergia grant EPISODE and individual grants.

REFERENCES

- (1) Kojima, A.; Teshima, K.; Shirai, Y.; Miyasaka, T. Organometal Halide Perovskites as Visible-Light Sensitizers for Photovoltaic Cells. *J. Am. Chem. Soc.* **2009**, *131*, 6050–6051.
- (2) Jeon, N. J.; Na, H.; Jung, E. H.; Yang, T.-Y.; Lee, Y. G.; Kim, G.; Shin, H.-W.; Il Seok, S.; Lee, J.; Seo, J. A Fluorene-Terminated Hole-Transporting Material for Highly Efficient and Stable Perovskite Solar Cells. *Nat. Energy* **2018**, *3*, 682–689.
- (3) Stranks, S. D.; Eperon, G. E.; Grancini, G.; Menelaou, C.; Alcocer, M. J. P.; Leijtens, T.; Herz, L. M.; Petrozza, A.; Snaith, H. J. Electron-Hole Diffusion Lengths Exceeding 1 Micrometer in an

Organometal Trihalide Perovskite Absorber. *Science* **2013**, *342*, 341–344.

(4) Wehrenfennig, C.; Eperon, G. E.; Johnston, M. B.; Snaith, H. J.; Herz, L. M. High Charge Carrier Mobilities and Lifetimes in Organolead Trihalide Perovskites. *Adv. Mater.* **2014**, *26*, 1584–1589.

(5) Shi, D.; Adinolfi, V.; Comin, R.; Yuan, M.; Alarousu, E.; Buin, A.; Chen, Y.; Hoogland, S.; Rothenberger, A.; Katsiev, K.; Losovyj, Y.; Zhang, X.; Dowben, P. A.; Mohammed, O. F.; Sargent, E. H.; Bakr, O. M. Low Trap-State Density and Long Carrier Diffusion in Organolead Trihalide Perovskite Single Crystals. *Science* **2015**, *347*, 519–522.

(6) Dong, Q.; Fang, Y.; Shao, Y.; Mulligan, P.; Qiu, J.; Cao, L.; Huang, J. Electron-Hole Diffusion Lengths > 175 nm in Solution-Grown CH₃NH₃PbI₃ Single Crystals. *Science* **2015**, *347*, 967–970.

(7) Grätzel, M. The Light and Shade of Perovskite Solar Cells. *Nat. Mater.* **2014**, *13*, 838–842.

(8) Seok, S. I.; Grätzel, M.; Park, N.-G. Methodologies toward Highly Efficient Perovskite Solar Cells. *Small* **2018**, *14*, 1704177.

(9) Shockley, W.; Queisser, H. J. Detailed Balance Limit of Efficiency of *P n* Junction Solar Cells. *J. Appl. Phys.* **1961**, *32*, 510–519.

(10) Stoumpos, C. C.; Malliakas, C. D.; Kanatzidis, M. G. Semiconducting Tin and Lead Iodide Perovskites with Organic Cations: Phase Transitions, High Mobilities, and Near-Infrared Photoluminescent Properties. *Inorg. Chem.* **2013**, *52*, 9019–9038.

(11) Jeon, N. J.; Noh, J. H.; Kim, Y. C.; Yang, W. S.; Ryu, S.; Seok, S. I. Solvent Engineering for High-Performance Inorganic–Organic Hybrid Perovskite Solar Cells. *Nat. Mater.* **2014**, *13*, 897–903.

(12) Eperon, G. E.; Stranks, S. D.; Menelaou, C.; Johnston, M. B.; Herz, L. M.; Snaith, H. J. Formamidinium Lead Trihalide: A Broadly Tunable Perovskite for Efficient Planar Heterojunction Solar Cells. *Energy Environ. Sci.* **2014**, *7*, 982.

(13) Pellet, N.; Gao, P.; Gregori, G.; Yang, T.-Y.; Nazeeruddin, M. K.; Maier, J.; Grätzel, M. Mixed–Organic–Cation Perovskite Photovoltaics for Enhanced Solar-Light Harvesting. *Angew. Chem., Int. Ed.* **2014**, *53*, 3151–3157.

(14) Ji, F.; Wang, L.; Pang, S.; Gao, P.; Xu, H.; Xie, G.; Zhang, J.; Cui, G. A Balanced Cation Exchange Reaction toward Highly Uniform and Pure Phase FA_{1-x}MA_xPbI₃ Perovskite Films. *J. Mater. Chem. A* **2016**, *4*, 14437–14443.

(15) Prochowicz, D.; Yadav, P.; Saliba, M.; Sasaki, M.; Zakeeruddin, S. M.; Lewiński, J.; Grätzel, M. Mechanochemical Synthesis of Pure Phase Mixed–Cation MA_xFA_{1-x}PbI₃ Hybrid Perovskites: Photovoltaic Performance and Electrochemical Properties. *Sustain. Energy Fuels* **2017**, *1*, 689–693.

(16) Liu, T.; Zong, Y.; Zhou, Y.; Yang, M.; Li, Z.; Game, O. S.; Zhu, K.; Zhu, R.; Gong, Q.; Padture, N. P. High-Performance Formamidinium-Based Perovskite Solar Cells via Microstructure-Mediated δ -to- α Phase Transformation. *Chem. Mater.* **2017**, *29*, 3246–3250.

(17) Lee, J.-W.; Kim, D.-H.; Kim, H.-S.; Seo, S.-W.; Cho, S. M.; Park, N.-G. Formamidinium and Cesium Hybridization for Photo- and Moisture-Stable Perovskite Solar Cell. *Adv. Energy Mater.* **2015**, *5*, 1501310.

(18) Yi, C.; Luo, J.; Meloni, S.; Boziki, A.; Ashari-Astani, N.; Grätzel, M.; Zakeeruddin, S. M.; Röthlisberger, U.; Grätzel, M. Entropic Stabilization of Mixed A-Cation ABX₃ Metal Halide Perovskites for High Performance Perovskite Solar Cells. *Energy Environ. Sci.* **2016**, *9*, 656–662.

(19) Yang, Z.; Chueh, C.-C.; Liang, P.-W.; Crump, M.; Lin, F.; Zhu, Z.; Jen, A. K.-Y. Effects of Formamidinium and Bromide Ion Substitution in Methylammonium Lead Triiodide toward High-Performance Perovskite Solar Cells. *Nano Energy* **2016**, *22*, 328–337.

(20) Prochowicz, D.; Yadav, P.; Saliba, M.; Kubicki, D. J.; Tavakoli, M. M.; Zakeeruddin, S. M.; Lewiński, J.; Emsley, L.; Grätzel, M. One-Step Mechanochemical Incorporation of an Insoluble Cesium Additive for High Performance Planar Heterojunction Solar Cells. *Nano Energy* **2018**, *49*, 523–528.

(21) Chen, P.; Bai, Y.; Lyu, M.; Yun, J.-H.; Hao, M.; Wang, L. Progress and Perspective in Low-Dimensional Metal Halide Perovskites for Optoelectronic Applications. *Sol. RRL* **2018**, *2*, 1700186.

(22) Etgar, L. The Merit of Perovskite's Dimensionality; Can This Replace the 3D Halide Perovskite? *Energy Environ. Sci.* **2018**, *11*, 234–242.

(23) Yan, J.; Qiu, W.; Wu, G.; Heremans, P.; Chen, H. Recent Progress in 2D/Quasi-2D Layered Metal Halide Perovskites for Solar Cells. *J. Mater. Chem. A* **2018**, *6*, 11063–11077.

(24) Ma, C.; Leng, C.; Ji, Y.; Wei, X.; Sun, K.; Tang, L.; Yang, J.; Luo, W.; Li, C.; Deng, Y.; Feng, S.; Shen, J.; Lu, S.; Du, C.; Shi, H. 2D/3D Perovskite Hybrids as Moisture-Tolerant and Efficient Light Absorbers for Solar Cells. *Nanoscale* **2016**, *8*, 18309–18314.

(25) Yao, K.; Wang, X.; Xu, Y.; Li, F. A General Fabrication Procedure for Efficient and Stable Planar Perovskite Solar Cells: Morphological and Interfacial Control by in-Situ-Generated Layered Perovskite. *Nano Energy* **2015**, *18*, 165–175.

(26) Smith, I. C.; Hoke, E. T.; Solis-Ibarra, D.; McGehee, M. D.; Karunadasa, H. I. A Layered Hybrid Perovskite Solar-Cell Absorber with Enhanced Moisture Stability. *Angew. Chem.* **2014**, *126*, 11414–11417.

(27) Bai, Y.; Xiao, S.; Hu, C.; Zhang, T.; Meng, X.; Lin, H.; Yang, Y.; Yang, S. Dimensional Engineering of a Graded 3D-2D Halide Perovskite Interface Enables Ultrahigh V_{oc} Enhanced Stability in the p-i-n Photovoltaics. *Adv. Energy Mater.* **2017**, *7*, 1701038.

(28) Chen, P.; Bai, Y.; Wang, S.; Lyu, M.; Yun, J.-H.; Wang, L. In Situ Growth of 2D Perovskite Capping Layer for Stable and Efficient Perovskite Solar Cells. *Adv. Funct. Mater.* **2018**, *28*, 1706923.

(29) Cao, D. H.; Stoumpos, C. C.; Farha, O. K.; Hupp, J. T.; Kanatzidis, M. G. 2D Homologous Perovskites as Light-Absorbing Materials for Solar Cell Applications. *J. Am. Chem. Soc.* **2015**, *137*, 7843–7850.

(30) Stoumpos, C. C.; Cao, D. H.; Clark, D. J.; Young, J.; Rondinelli, J. M.; Jang, J. I.; Hupp, J. T.; Kanatzidis, M. G. Ruddlesden-Popper Hybrid Lead Iodide Perovskite 2D Homologous Semiconductors. *Chem. Mater.* **2016**, *28*, 2852–2867.

(31) Zhang, X.; Munir, R.; Xu, Z.; Liu, Y.; Tsai, H.; Nie, W.; Li, J.; Niu, T.; Smilgies, D.-M.; Kanatzidis, M. G.; Mohite, A. D.; Zhao, K.; Amassian, A.; Liu, S. F. Phase Transition Control for High Performance Ruddlesden-Popper Perovskite Solar Cells. *Adv. Mater.* **2018**, *30*, 1707166.

(32) Li, X.; Ibrahim Dar, M.; Yi, C.; Luo, J.; Tschumi, M.; Zakeeruddin, S. M.; Nazeeruddin, M. K.; Han, H.; Grätzel, M. Improved Performance and Stability of Perovskite Solar Cells by Crystal Crosslinking with Alkylphosphonic Acid ω -Ammonium Chlorides. *Nat. Chem.* **2015**, *7*, 703–711.

(33) Zhang, T.; Xie, L.; Chen, L.; Guo, N.; Li, G.; Tian, Z.; Mao, B.; Zhao, Y. In Situ Fabrication of Highly Luminescent Bifunctional Amino Acid Crosslinked 2D/3D NH₃C₄H₉COO(CH₃NH₃PbBr₃)_n Perovskite Films. *Adv. Funct. Mater.* **2017**, *27*, 1603568.

(34) Grancini, G.; Roldán-Carmona, C.; Zimmermann, I.; Mosconi, E.; Lee, X.; Martineau, D.; Narbey, S.; Oswald, F.; De Angelis, F.; Graetzel, M.; Nazeeruddin, M. K. One-Year Stable Perovskite Solar Cells by 2D/3D Interface Engineering. *Nat. Commun.* **2017**, *8*, 15684.

(35) Kayesh, Md. E.; Matsuishi, K.; Kaneko, R.; Kazaoui, S.; Lee, J.-J.; Noda, T.; Islam, A. Coadditive Engineering with 5-Ammonium Valeric Acid Iodide for Efficient and Stable Sn Perovskite Solar Cells. *ACS Energy Lett.* **2019**, *4*, 278–284.

(36) Ye, T.; Bruno, A.; Han, G.; Koh, T. M.; Li, J.; Jamaludin, N. F.; Soci, C.; Mhaisalkar, S. G.; Leong, W. L. Efficient and Ambient-Air-Stable Solar Cell with Highly Oriented 2D@3D Perovskites. *Adv. Funct. Mater.* **2018**, *28*, 1801654.

(37) Hu, Y.; Zhang, Z.; Mei, A.; Jiang, Y.; Hou, X.; Wang, Q.; Du, K.; Rong, Y.; Zhou, Y.; Xu, G.; Han, H. Improved Performance of Printable Perovskite Solar Cells with Bifunctional Conjugated Organic Molecule. *Adv. Mater.* **2018**, *30*, 1705786.

(38) Pan, J.; Shang, Y.; Yin, J.; De Bastiani, M.; Peng, W.; Dursun, I.; Sinatra, L.; El-Zohry, A. M.; Hedhili, M. N.; Emwas, A.-H.; Mohammed, O. F.; Ning, Z.; Bakr, O. M. Bidentate Ligand-Passivated

CsPbI₃ Perovskite Nanocrystals for Stable Near-Unity Photoluminescence Quantum Yield and Efficient Red Light-Emitting Diodes. *J. Am. Chem. Soc.* **2018**, *140*, 562–565.

(39) Krieg, F.; Ochsenbein, S. T.; Yakunin, S.; ten Brinck, S.; Aellen, P.; Süess, A.; Clerc, B.; Guggisberg, D.; Nazarenko, O.; Shynkarenko, Y.; Kumar, S.; Shih, C.-J.; Infante, I.; Kovalenko, M. V. Colloidal CsPbX₃ (X = Cl, Br, I) Nanocrystals 2.0: Zwitterionic Capping Ligands for Improved Durability and Stability. *ACS Energy Lett.* **2018**, *3*, 641–646.

(40) Zheng, X.; Troughton, J.; Gasparini, N.; Lin, Y.; Wei, M.; Hou, Y.; Liu, J.; Song, K.; Chen, Z.; Yang, C.; Turedi, B.; Alsalloum, A. Y.; Pan, J.; Chen, J.; Zhumekenov, A. A.; Anthopoulos, T. D.; Han, Y.; Baran, D.; Mohammed, O. F.; Sargent, E. H.; Bakr, O. M. Quantum Dots Supply Bulk- and Surface-Passivation Agents for Efficient and Stable Perovskite Solar Cells. *Joule* **2019**, *3*, 1963–1976.

(41) Li, G.; Zhang, T.; Xu, F.; Zhao, Y. A Facile Deposition of Large Grain and Phase Pure α -FAPbI₃ for Perovskite Solar Cells via a Flash Crystallization. *Mater. Today Energy* **2017**, *5*, 293–298.

(42) Niu, T.; Lu, J.; Tang, M.-C.; Barrit, D.; Smilgies, D.-M.; Yang, Z.; Li, J.; Fan, Y.; Luo, T.; McCulloch, I.; Amassian, A.; Liu, S. F.; Zhao, K. High Performance Ambient-Air-Stable FAPbI₃ Perovskite Solar Cells with Molecule-Passivated Ruddlesden-Popper/3D Heterostructured Film. *Energy Environ. Sci.* **2018**, *11*, 3358–3366.

(43) Snaith, H. J.; Abate, A.; Ball, J. M.; Eperon, G. E.; Leijtens, T.; Noel, N. K.; Stranks, S. D.; Wang, J. T.-W.; Wojciechowski, K.; Zhang, W. Anomalous Hysteresis in Perovskite Solar Cells. *J. Phys. Chem. Lett.* **2014**, *5*, 1511–1515.

(44) Shih, Y.-C.; Lan, Y.-B.; Li, C.-S.; Hsieh, H.-C.; Wang, L.; Wu, C.-I.; Lin, K.-F. Amino-Acid-Induced Preferential Orientation of Perovskite Crystals for Enhancing Interfacial Charge Transfer and Photovoltaic Performance. *Small* **2017**, *13*, 1604305.

(45) Kanemitsu, Y. Luminescence Spectroscopy of Lead-Halide Perovskites: Materials Properties and Application as Photovoltaic Devices. *J. Mater. Chem. C* **2017**, *5*, 3427–3437.

(46) Prochowicz, D.; Franckevičius, M.; Cieślak, A. M.; Zakeeruddin, S. M.; Grätzel, M.; Lewiński, J. Mechanochemical Synthesis of the Hybrid Perovskite CH₃NH₃PbI₃: Characterization and the Corresponding Solar Cell Efficiency. *J. Mater. Chem. A* **2015**, *3*, 20772–20777.

(47) Rosales, B. A.; Wei, L.; Vela, J. Synthesis and Mixing of Complex Halide Perovskites by Solvent-Free Solid-State Methods. *J. Solid State Chem.* **2019**, *271*, 206–215.

(48) Rosales, B. A.; Men, L.; Cady, S. D.; Hanrahan, M. P.; Rossini, A. J.; Vela, J. Persistent Dopants and Phase Segregation in Organolead Mixed-Halide Perovskites. *Chem. Mater.* **2016**, *28*, 6848–6859.

(49) Roiland, C.; Trippé-Allard, G.; Jemli, K.; Alonso, B.; Ameline, J.-C.; Gautier, R.; Bataille, T.; Le Pollès, L.; Deleporte, E.; Even, J.; Katan, C. Multinuclear NMR as a Tool for Studying Local Order and Dynamics in CH₃NH₃PbX₃ (X = Cl, Br, I) Hybrid Perovskites. *Phys. Chem. Chem. Phys.* **2016**, *18*, 27133–27142.

(50) Kubicki, D. J.; Prochowicz, D.; Hofstetter, A.; Péchy, P.; Zakeeruddin, S. M.; Grätzel, M.; Emsley, L. Cation Dynamics in Mixed-Cation (MA)_x(FA)_{1-x}PbI₃ Hybrid Perovskites from Solid-State NMR. *J. Am. Chem. Soc.* **2017**, *139*, 10055–10061.

(51) Kubicki, D. J.; Prochowicz, D.; Hofstetter, A.; Zakeeruddin, S. M.; Grätzel, M.; Emsley, L. Phase Segregation in Cs-, Rb- and K-Doped Mixed-Cation (MA)_x(FA)_{1-x}PbI₃ Hybrid Perovskites from Solid-State NMR. *J. Am. Chem. Soc.* **2017**, *139*, 14173–14180.

(52) Fabini, D. H.; Siaw, T. A.; Stoumpos, C. C.; Laurita, G.; Olds, D.; Page, K.; Hu, J. G.; Kanatzidis, M. G.; Han, S.; Seshadri, R. Universal Dynamics of Molecular Reorientation in Hybrid Lead Iodide Perovskites. *J. Am. Chem. Soc.* **2017**, *139*, 16875–16884.

(53) Kubicki, D. J.; Prochowicz, D.; Hofstetter, A.; Zakeeruddin, S. M.; Grätzel, M.; Emsley, L. Phase Segregation in Potassium-Doped Lead Halide Perovskites from ³⁹K Solid-State NMR at 21.1 T. *J. Am. Chem. Soc.* **2018**, *140*, 7232–7238.

(54) Karmakar, A.; Askar, A. M.; Bernard, G. M.; Terskikh, V. V.; Ha, M.; Patel, S.; Shankar, K.; Michaelis, V. K. Mechanochemical Synthesis of Methylammonium Lead Mixed-Halide Perovskites:

Unraveling the Solid-Solution Behavior Using Solid-State NMR. *Chem. Mater.* **2018**, *30*, 2309–2321.

(55) Karmakar, A.; Dodd, M. S.; Agnihotri, S.; Ravera, E.; Michaelis, V. K. Cu(II)-Doped Cs₂SbAgCl₆ Double Perovskite: A Lead-Free, Low-Bandgap Material. *Chem. Mater.* **2018**, *30*, 8280–8290.

(56) Franssen, W. M. J.; Bruijnaers, B. J.; Portengen, V. H. L.; Kentgens, A. P. M. Dimethylammonium Incorporation in Lead Acetate Based MAPbI₃ Perovskite Solar Cells. *ChemPhysChem* **2018**, *19*, 3107–3115.

(57) Kubicki, D. J.; Prochowicz, D.; Hofstetter, A.; Saski, M.; Yadav, P.; Bi, D.; Pellet, N.; Lewiński, J.; Zakeeruddin, S. M.; Grätzel, M.; Emsley, L. Formation of Stable Mixed Guanidinium-Methylammonium Phases with Exceptionally Long Carrier Lifetimes for High-Efficiency Lead Iodide-Based Perovskite Photovoltaics. *J. Am. Chem. Soc.* **2018**, *140*, 3345–3351.

(58) Askar, A. M.; Karmakar, A.; Bernard, G. M.; Ha, M.; Terskikh, V. V.; Wiltshire, B. D.; Patel, S.; Fleet, J.; Shankar, K.; Michaelis, V. K. Composition-Tunable Formamidinium Lead Mixed Halide Perovskites via Solvent-Free Mechanochemical Synthesis: Decoding the Pb Environments Using Solid-State NMR Spectroscopy. *J. Phys. Chem. Lett.* **2018**, *9*, 2671–2677.

(59) Franssen, W. M. J.; Kentgens, A. P. M. Solid-State NMR of Hybrid Halide Perovskites. *Solid State Nucl. Magn. Reson.* **2019**, *100*, 36–44.

(60) Kubicki, D. J.; Prochowicz, D.; Pinon, A.; Stevanato, G.; Hofstetter, A.; Zakeeruddin, S. M.; Grätzel, M.; Emsley, L. Doping and Phase Segregation in Mn²⁺- and Co²⁺-Doped Lead Halide Perovskites from ¹³³Cs and ¹H NMR Relaxation Enhancement. *J. Mater. Chem. A* **2019**, *7*, 2326–2333.

(61) Xiang, W.; Wang, Z.; Kubicki, D. J.; Tress, W.; Luo, J.; Prochowicz, D.; Akin, S.; Emsley, L.; Zhou, J.; Dietler, G.; Grätzel, M.; Hagfeldt, A. Europium-Doped CsPbI₂Br for Stable and Highly Efficient Inorganic Perovskite Solar Cells. *Joule* **2019**, *3*, 205–214.

(62) Bi, D.; Li, X.; Milić, J. V.; Kubicki, D. J.; Pellet, N.; Luo, J.; LaGrange, T.; Mettraux, P.; Emsley, L.; Zakeeruddin, S. M.; Grätzel, M. Multifunctional Molecular Modulators for Perovskite Solar Cells with over 20% Efficiency and High Operational Stability. *Nat. Commun.* **2018**, *9*, 4482.

(63) Tavakoli, M. M.; Tress, W.; Milić, J. V.; Kubicki, D.; Emsley, L.; Grätzel, M. Addition of Adamantylammonium Iodide to Hole Transport Layers Enables Highly Efficient and Electroluminescent Perovskite Solar Cells. *Energy Environ. Sci.* **2018**, *11*, 3310–3320.

(64) Milić, J. V.; Im, J.; Kubicki, D. J.; Ummadisingu, A.; Seo, J.; Li, Y.; Ruiz Preciado, M. A.; Dar, M. I.; Zakeeruddin, S. M.; Emsley, L.; Grätzel, M. Supramolecular Engineering for Formamidinium Based Layered 2D Perovskite Solar Cells: Structural Complexity and Dynamics Revealed by Solid State NMR Spectroscopy. *Adv. Energy Mater.* **2019**, *9*, 1900284.

(65) Chen, J.; Seo, J.-Y.; Park, N.-G. Simultaneous Improvement of Photovoltaic Performance and Stability by In Situ Formation of 2D Perovskite at (FAPbI₃)_{0.88}(CsPbBr₃)_{0.12}/CuSCN Interface. *Adv. Energy Mater.* **2018**, *8*, 1702714.

(66) Willett, R. D.; Maxcy, K. R.; Twamley, B. Polytypism in Columnar Group 14 Halide Salts: Structures of (Et₂NH₂)₃Pb₃X₉ · nH₂O (X = Cl, Br) and (β-Alanine)₂Sn₄. *Inorg. Chem.* **2002**, *41*, 7024–7030.

(67) Elena, B.; Pintacuda, G.; Mifsud, N.; Emsley, L. Molecular Structure Determination in Powders by NMR Crystallography from Proton Spin Diffusion. *J. Am. Chem. Soc.* **2006**, *128*, 9555–9560.

(68) Ke, W.; Stoumpos, C. C.; Zhu, M.; Mao, L.; Spanopoulos, I.; Liu, J.; Kontsevoi, O. Y.; Chen, M.; Sarma, D.; Zhang, Y.; Wasielewski, M. R.; Kanatzidis, M. G. Enhanced Photovoltaic Performance and Stability with a New Type of Hollow 3D Perovskite {en}FASnI₃. *Sci. Adv.* **2017**, *3*, No. e1701293.

(69) Spanopoulos, I.; Ke, W.; Stoumpos, C. C.; Schueller, E. C.; Kontsevoi, O. Y.; Seshadri, R.; Kanatzidis, M. G. Unraveling the Chemical Nature of the 3D “Hollow” Hybrid Halide Perovskites. *J. Am. Chem. Soc.* **2018**, *140*, 5728–5742.

(70) *NMR of Quadrupolar Nuclei in Solid Materials*; Wasylshen, R. E., Ashbrook, S. E., Wimperis, S., Eds.; Wiley: Hoboken, NJ, 2012.

(71) Long, J. R.; Sun, B. Q.; Bowen, A.; Griffin, R. G. Molecular Dynamics and Magic Angle Spinning NMR. *J. Am. Chem. Soc.* **1994**, *116*, 11950–11956.

(72) Mercier, N. $(\text{HO}_2\text{C}(\text{CH}_2)_3\text{NH}_3)_2(\text{CH}_3\text{NH}_3)\text{Pb}_2\text{I}_7$: A Predicted Non-Centrosymmetrical Structure Built up from Carboxylic Acid Supramolecular Synthons and Bilayer Perovskite Sheets. *CrystEngComm* **2005**, *7*, 429.

(73) Li, T.; Dunlap-Shohl, W. A.; Reinheimer, E. W.; Le Magueres, P.; Mitzi, D. B. Melting Temperature Suppression of Layered Hybrid Lead Halide Perovskites via Organic Ammonium Cation Branching. *Chem. Sci.* **2019**, *10*, 1168–1175.

(74) Fu, Y.; Wu, T.; Wang, J.; Zhai, J.; Shearer, M. J.; Zhao, Y.; Hamers, R. J.; Kan, E.; Deng, K.; Zhu, X.-Y.; Jin, S. Stabilization of the Metastable Lead Iodide Perovskite Phase via Surface Functionalization. *Nano Lett.* **2017**, *17*, 4405–4414.

■ NOTE ADDED IN PROOF

While the article was in press, we became aware of a study using BA, PEA, and 4-fluorophenylethylammonium hydroiodides to stabilize the 3D perovskite structure of FAPbI₃ in nanostructures and thin films, which we have now referenced for completeness.⁷⁴